Finite temperature effects on the X-ray absorption spectra of lithium compounds: First-principles interpretation of X-ray Raman measurements

Tod A. Pascal,[1] Ulrike Boesenberg,[2,a)] Robert Kostecki,[2] Thomas J. Richardson,[2] Tsu-Chien Weng,[3] Dimosthenis Sokaras,[3] Dennis Nordlund,[3] Eamon McDermott,[4] Alexander Moewes,[4] Jordi Cabana,[2,5] and David Prendergast[1,b)]

[1]*The Molecular Foundry, Materials Science Division, Lawrence Berkeley National Laboratory (LBNL), Berkeley, California 94720, USA*
[2]*Environmental Energy Technologies Division, LBNL, Berkeley, California 94720, USA*
[3]*Stanford Synchrotron Radiation Lightsource, SLAC National Accelerator Laboratory, Stanford, California 94720, USA*
[4]*University of Saskatchewan, Department of Physics and Engineering Physics, Saskatoon, Saskatchewan S7N 5E2, Canada*
[5]*Department of Chemistry, University of Illinois at Chicago, Chicago, Illinois 60605, USA*

We elucidate the role of room-temperature-induced instantaneous structural distortions in the Li K-edge X-ray absorption spectra (XAS) of crystalline LiF, Li_2SO_4, Li_2O, Li_3N, and Li_2CO_3 using high resolution X-ray Raman spectroscopy (XRS) measurements and first-principles density functional theory calculations within the eXcited electron and Core Hole approach. Based on thermodynamic sampling via *ab initio* molecular dynamics simulations, we find calculated XAS in much better agreement with experiment than those computed using the rigid crystal structure alone. We show that local instantaneous distortion of the atomic lattice perturbs the symmetry of the Li $1s$ core-excited-state electronic structure, broadening spectral line-shapes and, in some cases, producing additional spectral features. The excellent agreement with high-resolution XRS measurements validates the accuracy of our first-principles approach to simulating XAS, and provides both accurate benchmarks for model compounds and a predictive theoretical capability for identification and characterization of multi-component systems, such as lithium-ion batteries, under working conditions. © *2014 AIP Publishing LLC.* [http://dx.doi.org/10.1063/1.4856835]

I. INTRODUCTION

Lithium is an abundant element with low mass and high mobility, making it attractive as a component in chemical[1,2] and electrochemical[3] energy storage technologies. Its low electronegativity and small ionic radius facilitate high reactivity and diverse chemical bonding and coordination in the solid state. Despite this versatility, large-scale adoption of lithium-based energy storage technologies depends critically on establishing sustained reversibility between the operational end states (e.g., charged-discharged states in a battery). Reversibility can be compromised by inefficiencies in the storage reaction or by competition from secondary reactions that consume reagents.[4] The creation of kinetically trapped species due to deficient cationic mobility[5] and the decomposition of the electrolyte on the surface of a battery electrode[6] are examples of the two general cases, respectively. Both mechanisms can also intertwine, e.g., when the charge transport through a solid layer resulting from electrolyte decomposition determines electrochemical performance.[7]

Rational design solutions, which maximize the utilization and life of these storage active materials, depend criti-

cally on an atomic-scale understanding of the reaction mechanisms and kinetics. Modern spectroscopic tools can probe vibrational and electronic degrees of freedom to elucidate the complex chemistry and physics in solids, and X-ray spectroscopies offer element-specific information by directly probing atomic core-levels of a given element present in the sample under study. X-ray absorption spectra (XAS), in particular, near-edge X-ray absorption fine structure (NEXAFS or XANES), can be interpreted as a map of element-specific, local, unoccupied electronic structure.[8,9] In this work, we focus on XAS excitation energies close to the Li $1s$ core-level absorption threshold (∼55–63 eV). Typically, direct, resonant soft-X-ray photon absorption is limited by attenuation to studies of extremely thin samples or surfaces, which presents obvious challenges for probing a buried electrochemically active interface *in situ*. X-ray Raman spectroscopy (XRS)[10] is a complimentary, bulk-sensitive technique, which measures inelastic scattering of an incoming beam of hard X rays (>5000 eV), focusing on energy losses in the energy region of a given elemental absorption edge. Previously, XRS measurements have been resolution-limited with respect to complimentary NEXAFS experiments. However, recent technical developments have enabled high resolution (∼0.3 eV) probing of materials with low absorption thresholds, such as lithium, using hard X-ray light sources.[11,12] With minimal momentum transfer, XRS can be considered equivalent to

a)Present address: Deutsches Elektronen Synchrotron, DESY, Notkestrasse 85, 22607 Hamburg, Germany.
b)Author to whom correspondence should be addressed. Electronic address: dgprendergast@lbl.gov

corresponding NEXAFS/XANES measurements, which are solely selective to electronic transitions that obey dipole-selection rules.[9]

The data collected during an XAS/XRS experiment include signatures of various electronic transitions from atomic core-levels to accessible unoccupied states as the energy is swept through an element's absorption edge. This signature is highly specific to a given compound, enabling the use of fingerprints from reference samples to identify chemical components of the system under study.[13, 14] However, reactions that are controlled by an electrochemical potential typically involve extreme conditions and chemical states that are challenging to prepare by any other methods. Further, signals can become extremely convoluted in the presence of multiple competing reactions that can each lead to a mixture of products; the simultaneous decomposition of non-aqueous electrolyte solvents during the lithiation of graphite[15, 16] or the oxygen reduction reaction by lithium[17] are canonical examples. These cases may limit the efficiency of experimental fingerprints in interpretation of measured spectra, and so, theoretical approaches to simulate and interpret XAS may be vital.[15]

In response to this, we have been developing a first-principles theoretical approach to interpret the XAS of complex materials. Our approach exploits an efficient occupation-constrained excited-state density functional theory approach, referred to as eXcited electron and Core-Hole (XCH).[18–20] In this work, we utilize the XCH approach to predict the spectra of a series of lithium compounds: LiF, Li_2SO_4, Li_2O, Li_3N, and Li_2CO_3. These compounds were selected as case examples for this proof-of-concept study, because they are relatively simple and known to be involved in reactions of relevance to electrochemistry[4, 6, 21] and hydrogen storage.[1, 22] In addition, we use configurational sampling from *ab initio* molecular dynamics (AIMD) simulations to quantify the effect of nuclear dynamics at finite temperature on the excited electronic states and associated spectral features. For comparison and validation, the experimental spectra were collected by high resolution XRS. These measurements are bulk-sensitive, reducing the effect of surface contamination in the measurements. Considering the chemical sensitivity of lithium compounds to the environment; such contamination can dominate surface-sensitive NEXAFS/XANES spectra, particularly where the signal is collected as total electron yield, and the electron mean-free-path may be limited to ∼1–10 nm. Our calculated XAS and measured XRS spectra are found to be in excellent agreement. Most significantly, our first-principles simulations show how the interplay between instantaneous distortions in the crystal lattice at finite temperature and the character of the ground state density of states conspire to activate dipole-forbidden pre-edge transitions in LiF, which is confirmed by our high resolution, bulk-sensitive XRS measurements. Energetic reordering of the lithium $1s$ excited states in other compounds is shown to preclude a similar pre-edge feature.

The remainder of this paper is arranged as follows: in Sec. II we present the theoretical and experimental approaches, followed by an interpretation of our results in Sec. III and a concluding summary in Sec. IV.

II. THEORETICAL AND EXPERIMENTAL APPROACHES

A. Theoretical methods

1. Simulating X-ray absorption

Our goal is to simulate the X-ray absorption cross section, $\sigma(\omega)$, of a given atomic structural model resonant with the core-level(s) of one of its constituent elements. Theoretical methods of accomplishing this all employ various approximations to Fermi's golden rule:

$$\sigma(\omega) = 4\pi^2\alpha_0\hbar\omega \sum_f |M_{i \to f}|^2 \delta(E_f - E_i - \hbar\omega), \quad (1)$$

where α_0 is the fine structure constant, $M_{i\text{->}f}$ are the transition matrix elements between the initial and final states, of energy E_i and E_f, respectively, and $\hbar\omega$ is the energy of the incoming photon which should match $E_f - E_i$. The electronic ground state (GS) of the system is assumed as the initial state.

Theoretical methods vary in their approximation of the many-body ground and core-excited final states and their corresponding transition matrix elements. In the context of modeling XAS in solid-state, periodic systems, approaches can be divided into two classes, which treat the core-excited atom and resultant excited-state electronic structure either as (1) an isolated embedded cluster or (2) as a periodic array of well-separated defects. The former class is typically limited to approaches employing a localized orbital representation of electronic structure and is common in the quantum chemistry community. The latter is more familiar to the solid-state physics community.

The localized nature of the core-excited state seems to favor both approaches, although the description of how localized states are embedded in a continuum of electronic states present in a periodic system is perhaps more readily describable in the latter. In either case, the particular physical approximation used to describe the core-excited state can vary from a many-body approach to a simpler effective-single-particle picture. Quantum-chemists favor the configuration interaction method and algorithmic modifications within that space,[23] while solid-state physicists often employ many-body perturbation theory to solve for electron-hole interactions using the Bethe-Salpeter equation.[24] However, in strongly correlated systems, where descriptions of core-excited states beyond single electron-hole pairs are necessary, hybrid approaches are required[25] which can adequately project periodic band structure onto cluster models that are amenable to exact diagonalization or configuration interaction.

However, if we limit ourselves to K-edge excitations (i.e., excitations from the $1s$ core of the element of interest), as in this work, then reasonable (and computationally much cheaper) approximations to XAS are possible using density functional theory (DFT), in which the core-excited state is modeled using the effective-single-particle (Kohn-Sham) basis of a perturbed Hamiltonian. This perturbation is introduced as an orbital occupation constraint within standard DFT, whereby the electron density is constructed from Kohn-Sham orbitals with modified occupations. In this context, the transition matrix elements are computed in the effective

single-particle approximation, using individual Kohn–Sham Density Functional Theory (KS-DFT) eigenstates, which couples the core-electron of the ground state with the accessible empty states of the final (core-excited) state:

$$M_{i \to f} = \langle \Psi_f | \hat{\varepsilon} \cdot R | \Psi_i \rangle \approx S \langle \psi_f | \hat{\varepsilon} \cdot r | \psi_i \rangle. \qquad (2)$$

In this expression, upper-case refers to many-body eigenstates and operators and lower-case refers to effective-single-particle analogs. Computational cost is typically reduced by modeling only the lowest-energy core-excited state, with the remaining orbitals generated non-self-consistently from the same self-consistent potential. In that approximation, the prefactor, S, above is assumed constant across all excitations.

There is a diverse spectrum of DFT-based approaches to modeling XAS, classified by the various approximations to the final state within KS-DFT. Early attempts to model the final state include: the $Z + 1$ approach,[26] which uses the ground state of a system in which the next element $(Z + 1)$ in the periodic table is substituted for the excited atom; transition potential calculations,[27] where the final states and energies are represented by the set of unoccupied orbitals derived from a self-consistent field in which "half" the core electron is excited – so-called Half-Core-Hole – a modified version of an approximation originally proposed by Slater;[28] and the full-core hole approach,[29] which models the full response of the unoccupied states to the presence of a core-hole.

In our approach, we follow the Delta-Self-Consistent-Field (ΔSCF) procedure to approximate the lowest energy, adiabatic, core-excited state within a constraint on orbital occupation, which we have dubbed the XCH method,[18] where the core hole produced by the absorption of an X-ray photon is introduced in the presence of the associated excited electron, placed in the lowest available unoccupied state, and the resulting self-consistent field is used to produce a spectrum of further excited (unoccupied) states. Others have used this approach in the solid-state context.[30,31] We adopted this approach due to its accuracy and transferability across a range of isolated and condensed-phase material contexts and its use of a formally neutral excited-state self-consistent charge density. Previous application to a molecular solid, ice Ih,[18] indicates that neither FCH nor HCH accurately reproduces the O K-edge XAS in the near-edge region, while the XCH approach captures the correct electronic response to localized excited states in which the excited electron effectively screens the core-hole from distant valence electrons.

Our calculations represent electronic structure using a plane-wave basis, employing periodic boundary conditions. This is an effective numerical approach to faithfully model crystalline phases; to approximate disordered condensed phases; or even to model finite systems, provided the unit cell (or supercell) is sufficiently large. Consequently, numerically converged XAS requires a dense sampling of electronic structure with respect to electron wave-vector in the first Brillouin zone (so-called k-point sampling).[19,32] To this end, an efficient generalization[33] of the k-space interpolation scheme for electronic structure presented by Shirley[34] can be used to calculate the k-dependent band structure from a given effective single-particle Hamiltonian at little extra computational cost.

This scheme increases the efficiency of our calculations by one to two orders of magnitude.

Our plane-wave calculations do not explicitly include core-electrons and use the pseudopotential approximation instead. Hence, the core-hole is ultimately modeled using a modified pseudopotential derived from an approximation to the core-excited atom which employs the same XCH orbital constraint described above. Known deficiencies in KS-DFT,[35] particularly the underestimation of bandgaps[36] and concomitantly bandwidths due to inaccurate quasiparticle (excitation) energies,[37] are also evident in simulated XAS. However, quantitative agreement with experiment is possible by uniformly stretching the energy axis of the resulting excited-state KS-DFT spectrum and we apply that approach here.

Recently, we have found that the inclusion of thermal effects by averaging over individual snapshots from molecular dynamics configurations greatly improves the agreement with experiment.[20,32,38] Sampling a thermodynamic ensemble in this way is similar in spirit to the actual experimental probe, which instantaneously samples many molecular configurations. Recent studies of the XAS of aqueous alanine and sarcosine[39] and pyrrole[32] using our XCH-MD approach have demonstrated that the inclusion of finite-temperature effects leads to much better agreement with experiment. Previous work has focused on the use of empirical force-fields, but here we adopt *ab initio* MD to model the finite-temperature dynamics of lithium compounds (see below).

2. Computational details

All our DFT calculations employ the PBE GGA functional.[40] Plane-wave pseudopotential calculations used ultrasoft pseudopotentials[41] and a kinetic energy cutoff for electronic wave functions (density) of 25 (200) Ry. The PWSCF code within the Quantum-ESPRESSO package[42] was used to generate the core-excited (XCH) Kohn–Sham eigenspectrum. Based on a numerically converged self-consistent charge density, we generated the unoccupied states for our XAS calculations non-self-consistently, sufficiently sampling the first Brillouin zone with a $5 \times 5 \times 5$ uniform k-point grid, employing an efficient implementation of the Shirley interpolation scheme[34] generalized to handle ultrasoft pseudopotentials.[33] Matrix elements were evaluated within the projector-augmented-wave (PAW) frozen-core approximation.[43] Core-excited ultrasoft pseudopotentials and corresponding atomic orbitals were generated with the Vanderbilt code.[41] Our excitation energies were convoluted with a 0.1 eV Gaussian function to produce continuous spectra. Due to underestimation of bandwidths by PBE, the resulting spectra were uniformly stretched by 10%–25% to improve experimental agreement (Table II). We calculated the average Li spectrum for each compound. For crystals, the spectrum of each symmetry-inequivalent lithium atom was determined, while for the thermally disordered MD snapshots, the spectra of all Li atoms were sampled. Large supercells (comprising multiple primitive cells) are employed so that the electronic excited state density around the excited atom is sufficiently contained in order to accurately model at least the

first core-excited state. Where computationally feasible, we verified that our simulated spectra were converged with respect to supercell size.

3. Alignment of calculated spectra using formation energies

Pseudopotentials are designed to reproduce valence electron scattering from the atomic nucleus and core electrons, reproducing the valence eigenenergies of an isolated atom, but they do not reproduce total energies due to the missing contributions of the core-electrons. Therefore, we cannot make quantitative comparisons between the energies of ground and core-excited systems within the pseudopotential approximation, since the core-excited (XCH) state is modeled using a substituted pseudopotential. Typically, simulated XAS from pseudopotential calculations include an empirical shift to align with experimental energy scales (or vice versa). Schematically, one can associate the calculated core-excited conduction band minimum or lowest unoccupied orbital energy with the measured absorption onset. While possibly sufficient for systems with spectra resulting from only one chemically unique atom, more complex systems require a predictive approach capable of providing the correct relative alignment between core-excited atoms in different chemical contexts.

Within the same supercell calculation, one can obtain an accurate relative alignment of the excitation energies of symmetry inequivalent atoms, by directly comparing the excited state total energies, since each involves the same numbers and types of atoms under the same periodic boundary conditions. When sampling snapshots from molecular dynamics trajectories, one can accurately align the spectra of atoms in different snapshots provided the periodic boundary conditions are fixed (constant volume and lattice constants). However, aligning spectra from systems with different boundary conditions, or differing numbers and types of atoms requires an alternative approach. Therefore, we have developed a method of aligning simulated XAS using pseudopotentials which references the excitation energies of an isolated atom under the same boundary conditions[20,44] while relying on one rigid shift in

energy to align with some measured reference system. Pickard and co-workers have independently developed a very similar approach.[45]

Our approach allows us to directly compare our calculated lithium K-edge spectra across various compounds with differing cell symmetries and volumes. This scheme has already proved effective for carbonates and carbon dioxide[20] and for copper oxides.[44] In this study, we chose lithium fluoride as our reference system and shift our calculated spectra by +56.75 eV to match the measured first major peak (this shift is unique to the pseudopotentials used in this study). We will show that we can predict the main peak of the remaining lithium compounds to within 0.2 eV by applying the same shift.

4. Ab initio Molecular Dynamics (AIMD)

Previous studies of the role of dynamics on spectra of condensed phase systems using the XCH approach relied on empirical interaction potentials (forcefields) that do not include charge polarization effects and strictly should not be assumed accurate in modeling systems not explicitly considered in the parameterization. AIMD overcome these two basic limitations of classical forcefields by accounting for the electronic degrees of freedom on the fly during the classical motion of the nuclei, although at significant computational cost. AIMD simulations are expected to be more accurate and transferable than classical forcefields, especially in modeling the dynamics of solids where the underlying DFT functional can reasonably describe the ground state density.

AIMD simulations were performed on supercells of the bulk solids (Table I). We used a modified version of the mixed Gaussian and plane wave code[46] CP2K/Quickstep.[47] We employed a triple-zeta basis set with two additional sets of polarization functions (TZV2P)[48] and a 320 Ry plane-wave cutoff. The unknown exchange-correlation potential is substituted by the PBE generalized gradient approximation[40] (consistent with our XAS simulations), and the Brillouin zone is sampled at the Γ-point only. Interactions between the valence electrons and the ionic cores are described by norm-conserving pseudopotentials.[49] The Poisson problem is

TABLE I. Description of systems for *ab initio* MD simulations and XCH calculations.

	Crystal symmetry	Primitive cell dimension $(a,b,c,\alpha,\beta,\gamma)$	Supercell	# of atoms	$\langle$MD cell$\rangle$	% cell expansion
LiF[57]	rock salt (cubic)	a = b = c = 4.028 Å, $\alpha = \beta = \gamma = 90$	$2 \times 2 \times 2$	64	a = b = c = 8.28 Å	5.4%
Li$_2$O[63]	anti-fluorite (tetrahedral)	a = b = c = 4.61 Å, $\alpha = \beta = \gamma = 90$	$2 \times 2 \times 2$	96	a = b = c = 9.41 Å	2.0%
Li$_3$N[67]	Hexagonal	a = b = 3.65 Å, c = 3.85, $\alpha = \beta = 90$, $\gamma = 120$	$3 \times 3 \times 3$	108	a = b = 10.99 Å, c = 11.68 Å	6.67%
α-Li$_2$SO$_4$[61]	Monoclinic	a = 8.24 Å, b = 4.95 Å, c = 8.47 Å, $\alpha = \gamma = 90$, $\beta = 107.98$	$2 \times 3 \times 2$	336	a = 17.04 Å, b = 15.37 Å, c = 17.53 Å	3.4%
Li$_2$CO$_3$[68]	Monoclinic	a = 8.35 Å, b = 4.97 Å, c = 6.20 Å, $\alpha = \gamma = 90$, $\beta = 114.83$	$2 \times 3 \times 3$	432	a = 17.08 Å, b = 15.26 Å, c = 18.60 Å	2.3%

tackled using an efficient Wavelet-based solver.[50] Equilibration simulations were run for at least 20 ps with a 0.5 fs time-step in the constant pressure (1 bar), constant temperature (298 K) ensemble, using a Nose-Hoover thermostat (damping constant of 100 fs) and an Andersen barostat (pressure damping constant of 2 ps). This was followed by 10 ps of constant volume, constant energy simulations. Snapshots of the system were saved every 2 ps (a total of 10 snapshots) for first-principles X-ray calculations.

B. Experimental X-ray Raman spectroscopy

A specially designed Swagelok-type cell with a 1 μm thick, 5×5 mm^2 Si$_3$N$_4$ membrane (Silson, Inc.) was used to probe bulk samples under inert conditions. All handling and storage of the air sensitive compounds was performed in an argon-filled glovebox with O$_2$ and H$_2$O levels below 1 ppm. Commercially available powders of LiF, Li$_2$SO$_4$, Li$_2$O, Li$_3$N, and Li$_2$CO$_3$ were used without purification.

X-ray Raman spectroscopy was carried out using the 40 crystal x-ray Raman spectrometer at beamline 6-2 at the Stanford Synchrotron Radiation Lightsource (SSRL).[12] With the beamline Si(311) monochromator and the spectrometer Si(440) reflection, an overall energy resolution of 0.3 eV was achieved. In order to minimize the non-dipole contributions, as well as the Compton scattering background within the Li XRS region, we used the three lowest momentum transfer columns of the spectrometer (0.86 Å^{-1}, 1.20 Å^{-1}, and 1.54 Å^{-1}, respectively); therefore, only 15 out of the 40 analyzers of the spectrometer were used for this study. The q$\langle r \rangle$ product within the exponential term of the scattering factor S(q,ω)[12] remained well below unity when accounting the Li 1s orbital mean radius ($\langle r \rangle = 0.18$ Å). When this exponent is Taylor expanded, the dipole term represents ~90% of its overall value. Neglecting the higher order terms a matrix element identical to Fermi's Golden Rule in direct soft-XAS is produced.[12] The higher order terms might give a small contribution from s-derived states in the XRS spectra (see, e.g., Ref. 13 for the sensitivity of s-derived state contribution to the momentum transfer q in XRS from Li$_2$O$_2$). The data were collected in reflection geometry with an incident angle of 8°. Multiple datasets were recorded for each sample and standard data processing was performed, e.g., normalization to the intensity of the incoming beam, averaging, background correction, and normalization to the edge jump.

III. RESULTS AND DISCUSSION

A. Lithium fluoride

As a first test case for accessing the ability of our XCH calculations to reproduce the experimental spectrum of lithium containing materials, we consider lithium fluoride (LiF), an ionic, colorless (14.1–14.5 eV bandgap[51]) solid that precipitates in the SEI of many Li-ion batteries, possibly from the breakdown and reaction of the PF$_6^-$ counterion with lithium.[52] At ambient pressures and temperatures, LiF exhibits a cubic, rock salt crystal structure (Fm-3m space group, a = 4.025 Å). Our measured XRS spectrum (Fig. 1) is
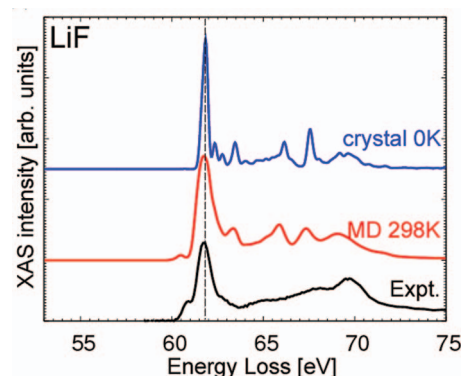

FIG. 1. X-ray absorption spectra of LiF from XRS measurements (black line) compared to XCH calculated spectrum using the static crystal (blue line) and the ensemble averaged spectrum using snapshots from an AIMD simulation at ambient conditions (red line). We shift the calculated spectra by +56.75 eV and dilated by 12% to better match experiment. Overall, the agreement to experiment is very good to excellent although the intensity of the higher energy features is underestimated. The spectrum from the MD snapshots is in better agreement to experiment and displays the prominent pre-edge feature at 61.5 eV that is absent in the spectrum of the perfect crystal.

relatively straightforward, with a main peak at 61.9 eV, some broad features from 63 to 64 eV, and a second peak around 70 eV, and is generally consistent with previous XANES and NEXAFS measurements.[13,53,54] Of particular interest, we find a prominent pre-edge shoulder (below 61.9 eV) in the XRS spectrum (this feature appears between 61.5 and 61.7 eV in previous XAS measurements). The origin of this feature has been discussed with some controversy in the literature. In one case, it has been proposed to arise from lattice vibrations, which break the crystal symmetry slightly, allowing electronic transitions to a nominally dark, strongly bound s-like exciton.[55] Alternatively, this feature is proposed to arise from quadrupole (q-dependent) contributions,[56] although we note that q-dependence cannot explain the appearance of this feature in resonant NEXAFS/XANES measurements,[13,54] since these techniques do not result in significant momentum transfer to enable quadrupole transitions at the Li K edge.

We performed electronic structure calculations on LiF using a $2 \times 2 \times 2$ supercell (64 atoms) of the cubic LiF crystal structure[57] (Table I). The first main peak in the experimental XRS spectrum is well resolved at 61.9 eV, so we applied a uniform shift of +56.2 eV in order to align our calculated XCH spectrum (this shift is unique to the pseudopotentials used in this study). The calculated XAS for the static crystal, i.e., the undistorted supercell, is in reasonable agreement with experiment (Fig. 1) and with previous BSE calculations using either pseudopotentials[13] or an all-electron formalism.[56] We note here that theoretical deficiencies of our DFT calculations lead to spectral widths that are too narrow (indeed, the DFT-PBE functional used in this work underestimates the valence bandgap of LiF by ~50%). We found that uniformly stretching our calculated spectra by a factor of 1.12 (Table II) greatly improved agreement with experiment, as accessed by numerical fitting of the two major peaks. Our calculations generally underestimate the oscillator strengths of excitations beyond the first main peak, possibly due to omission of momentum

TABLE II. Calculated chemical shifts of Lithium compounds after initial alignment with LiF (+56.75 eV). The DFT bandgaps and band-edges are underestimated compared to experiment, so we uniformly stretch our spectra to better match experiment.

	Expt. onset (ev)	Calc. onset crystal (eV)	Calc. onset MD (eV)	Expt. bandgap (eV)	DFT-PBE bandgap (eV)	Spectra stretching factor
LiF	60.17	60.17	60.17	14.1–14.5[a]	8.94	1.12
Li_2O	58.96	59.03	59.05	7.99[b]	4.25	1.25
Li_3N	55.00	54.93	54.95	1.3[c]	1.13	1.15
Li_2SO_4	58.46	59.04	58.22		6.7	1.30
Li_2CO_3	57.58	57.92	57.84		5.8	1.12
‖Error‖		0.21	0.13			

[a]Reference 51.
[b]Reference 69.
[c]Reference 64.

transfer (q-dependence),[56] although such non-dipole contributions should be small in our experiments, or from many-body excitations at higher energies. Additionally, the higher energy features of the calculated spectra appear sharper than the experiment possibly due to our use of a smaller (0.1 eV) numerical broadening than the estimated experimental resolution (0.3 eV).

Our calculated XAS using 10 snapshots from 298 K AIMD simulations (XCH-MD) is in better agreement with experiment. Here, we applied the same energy shift and dilation as for the static crystal. In the static crystal, the XCH density of states indicates that the first major peak at 61.9 eV arises from three degenerate *p*-like states (Fig. 2(a)). At finite temperature, we observe a breaking of the degeneracy into a broad distribution of states (Fig. 2(b)). In other words, finite temperature dynamics modify the energies of the excited electronic states to produce a distribution of energies which naturally broadens this spectral feature. In the past it has been typical to introduce effects due to thermal broadening in theoretical spectra by simple convolution with a Gaussian function, with an inherent assumption that individual electronic eigenenergies sample a normal distribution. By employing MD sampling, we make no such assumptions in our analysis, but instead allow the intrinsic degrees of freedom in these systems to define these distributions.

More importantly, we observe the appearance of a pre-edge feature at 61.5 eV in the XCH-MD spectrum; this feature is completely absent in the static crystal spectrum. To better understand the role of temperature in activating this pre-edge feature, we separately considered the character of each of the low energy excited states. As shown in Fig. 2(c), the lowest energy excited state in LiF is *s-like*, i.e., there is no node at the lithium nucleus for this state, in contrast to the *p*-like states that constitute the main edge (Figs. 2(c) and 2(d)). In the case of the static crystal, the electron probability distribution of the *s*-like state is centered on the excited lithium atom with a first moment equal to zero, i.e., this state has no *p*-character within a spatial volume that contains the lithium 1*s* core state. Optical excitations of the lithium 1*s* electron to this state are thus forbidden due to the dipole selection rules ($\Delta l = \pm 1$), meaning that this state is "dark." On the other hand, as shown in Fig. 2(d), a single snapshot sampled from our AIMD trajectory indicates that finite temperature instantaneous distortions can lead to broken inversion symmetry

about the excited lithium site and a distorted excited state that acquires *p*-character (i.e., develops a non-zero first moment) inside the volume spanned by the Li 1*s* electron. Since we assume that the Li 1*s* electron moves rigidly with the lithium nucleus, transitions to the distorted *s*-like state at finite temperature become "bright" and render that feature visible. We note that the energy of the pre-edge feature in our calculations is lower than that seen experimentally. This possibly arises from many-body effects that are not present in our effective single-particle approach. Specifically, in the symmetric LiF crystal, one might expect that exchange repulsion in the 1*s* -> 2*s* exciton would be stronger than in the 1*s* -> 2*p* case and this might in fact reduce the splitting in energy between these two transitions, increasing the absolute energy of the "*s*-like" pre-edge transition, bringing it closer to the main edge.

Population analysis of our AIMD simulation also reveals a fundamentally asymmetric Li–F bonding environment at finite temperature, where the nominally 2.01 Å Li–F bond splits into two distinct distributions centered at 1.95 Å and 2.13 Å (Fig. 2(d)). Integrating the area under the curve for each of the bimodal distributions, we find that there are on average four short and two long Li–F bonds at a given Li site at any time. Within a tight-binding approximation, one would expect *p*-state energies to increase (decrease) with decreasing (increasing) Li–F bond-length and the natural asymmetry of the bimodal distribution may well be the origin of the asymmetric line shape in the main peak. It clearly drives the intensity of the pre-edge feature, which relies on broken octahedral symmetry. This instantaneous asymmetric bonding predicted for LiF may be common to other rocksalt crystals. An unrelated temperature dependent neutron scattering study on lead chalcogenides (PbSe and PbTe) showed that with increasing temperature, entropic stabilization leads to two families of long and short bonds in these rock salt crystals.[58]

As noted above, NEXAFS and XANES measurements[13, 54] exhibit pre-edge features in the spectrum of LiF, and so the view that pre-edge features in LiF arise solely from quadrupole terms at high momentum transfer[56] appears insufficient. Indeed, our calculations indicate that finite temperature instantaneous distortion of the crystal structure is the origin of the pre-edge feature in the absence of quadrupole contributions, since our method does not include contributions beyond the dipole approximation. We note, however, that in previous NEXAFS and XANES
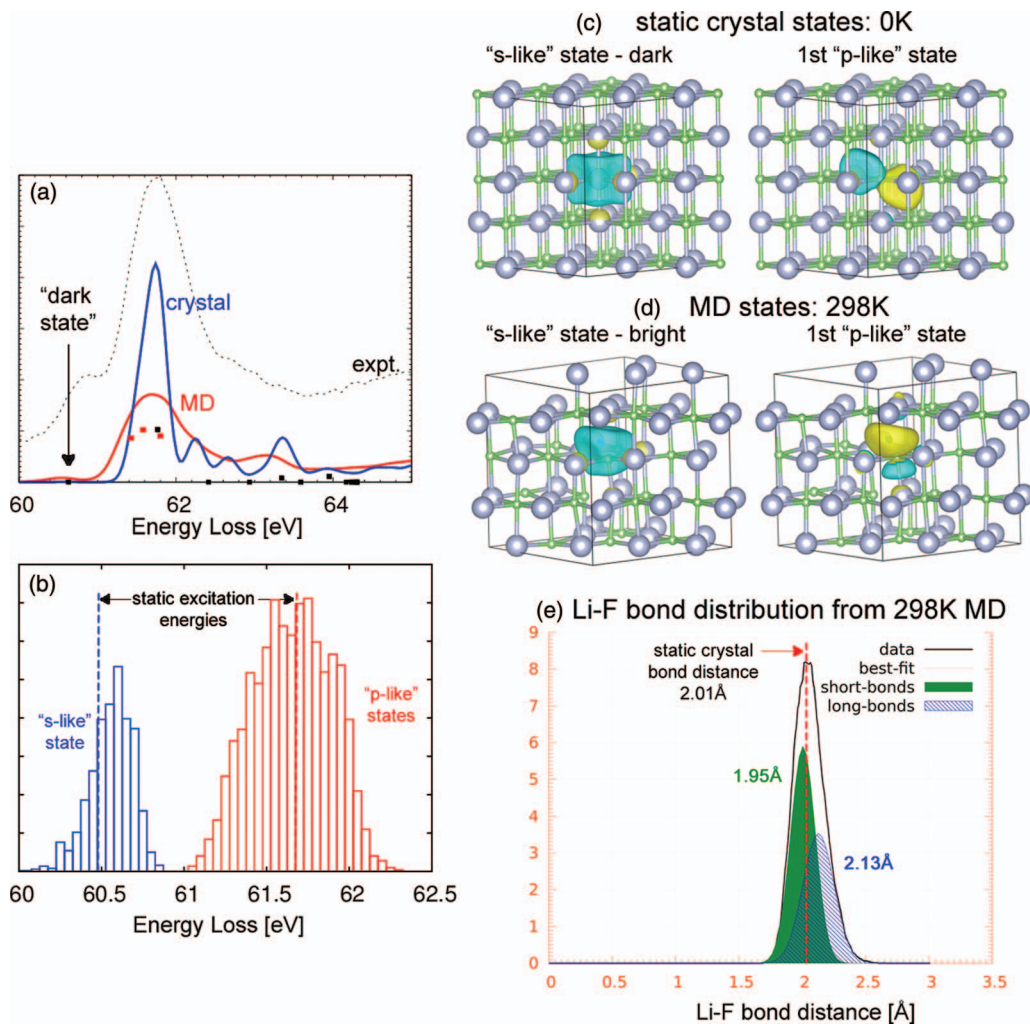
FIG. 2. (a) Comparison of the experimental (black dashed line) and calculated spectra using the static crystal (solid blue line) and snapshots from an AIMD simulations (solid red line). The squares represent the transition matrix elements that give rise to spectral features in the static crystal (blue) and MD averaged (red) structures. The excited electronic states that give rise to each spectral feature are indicated. Instantaneous distortion of the crystal lattice at finite temperature breaks the degeneracy of the 3 *p*-like states in the static crystal and produces a much broader spectrum that more closely matches experiment. The pre-edge feature at 61.5 eV is dark in the perfect crystal spectrum due to the dipole selection rules, but has some intensity at 298 K. (b) Distribution of the energies of the *s*-like (blue) and *p*-like (red) low energy excited states of LiF from XAS calculations on 10 snapshots of an AIMD simulation at 298 K (640 datapoints). The dashed lines represent the energy of the states from the static crystal. Molecular dynamics leads to broad distribution of the electronic excited state energies and shifts, with the average energy of the *s*-like state moving closer to the *p*-like states by 0.2 eV. (c) Representative electron density plot of the 1st (*s*-like) and 2nd (*p*-like) excited states in the static 0 K crystal. The lithium (green sphere) and fluorine atoms (light blue spheres) are shown. We adopt the convention that the positive phase of the density is colored magenta, while the negative phase is colored yellow. We only show 1 of the 3 *p*-like states. The symmetric *s*-like state is centered on the excited lithium atom. Excitation to this state is forbidden due to the dipole selection rules, meaning that this state is dark. (d) Representative electron density plot of the 1st and 2nd excited states of LiF from sampling every lithium in 10 independent snapshots of a 298 K AIMD simulations. Instantaneous distortions in the crystal lattice lead to an asymmetric, distorted excited state that overlaps with the lithium 1*s* electron and becomes "bright." Here, we show the excited lithium atom that contributes most to the pre-edge feature for demonstration purposes. (e) Distribution of every Li–F bond distances from 1000 snapshots in a 10 ps constant volume, constant energy (NVE) AIMD simulation. The bond lengths (black line) is best fitted by two independent Gaussian functions, so that the normally symmetric 2.01 Å Li–F bonds in the static crystal splits into two unique distributions at finite temperature: four "short" bonds centered at 1.95 Å (shaded solid green line) and two "long bonds" (shaded striped blue line) centered at 2.13 Å.

measurements,[13,54] the pre-edge intensity is much larger than that predicted by our calculations. To test the effect of temperature on the intensity of the pre-edge feature, we performed XCH/MD calculated at temperatures up to 500 K. These calculations, however, did not lead to a significantly greater pre-edge feature. This suggests that the more intense pre-edge feature observed experimentally likely arises from halide vacancies (color centers) induced by beam damage[59] or self-trapped excitons,[60] which would introduce static struc-

tural disorder, distorting the local octahedral coordination of Li sites – a proposition we are currently investigating.

B. Lithium sulfate

We now consider the XAS of another ionic lithium compound, Li_2SO_4, a white solid at room temperature. While the solid has monoclinic symmetry, each lithium atom has
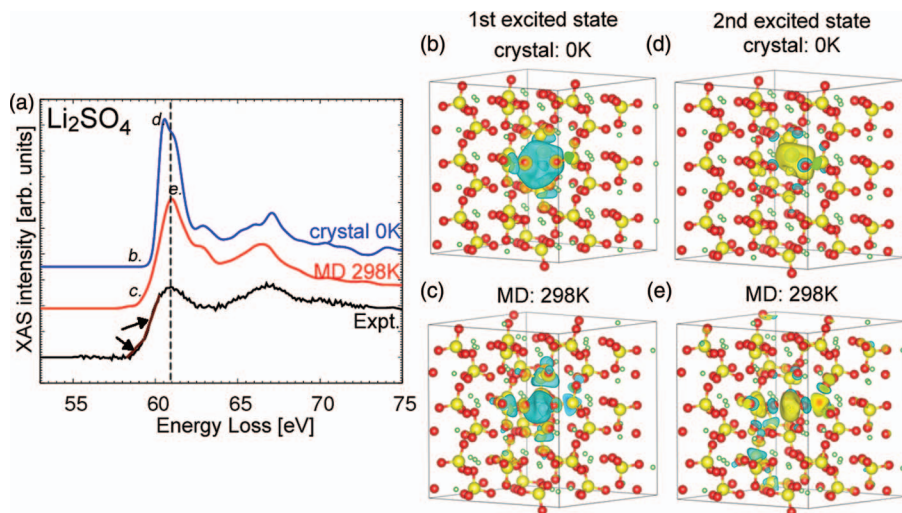
FIG. 3. (a) Comparison of the measured XRS spectrum of Li_2SO_4 (black line) with the XCH calculated spectrum using the static crystal (blue line) and the ensemble averaged spectrum from 298 K AIMD snapshots (red line). Similar to LiF, we find a low energy s-like state in the crystal that gives rise to a pre-edge feature at 58.5 eV at finite temperature but is absent from the static crystal. Our XRS spectrum shows a change in slope between 59.2 and 59.5 eV (as indicated by the black arrows) that may indicate the presence of this s-like state. (b) and (c) Representative first excited state of the static crystal and AIMD snapshots, respectively. The lithium (green), sulfur (yellow), and oxygen atoms (red) atoms are indicated. The color scheme for the states is the same as in Fig. 2. The s-like state acquires p-like at finite temperature to produce a pre-edge feature, similar to LiF. (d) and (e) Representative second, p-like excited state of the static crystal and finite temperature structure, respectively.

6 neighbors in a quasi-octahedral geometry.[61] For the purposes of this study, we focus on the most abundant alpha (α) phase. Previous studies have indicated that there is a phase transition to a "free rotor" phase above 848 K.[62] The experimental XRS spectrum at room temperature is again rather simple and similar to that of LiF: the first major peak lies at 61.72 eV and a second at 67.25 eV, with no other major features (Fig. 3(a)). Our calculated XCH spectrum using the static crystal reproduces the energies of these major peaks quite well, although similar to LiF, the relative intensity of the second major peak is underestimated compared to experiment. Again, this may be due to missing quadrupole transitions in our calculations. We note that by applying the same +56.75 eV shift as for LiF, we predict the first major peak at 60.9 eV, which is in excellent agreement with experiment (Table II).

The XAS calculated from the 10 MD snapshots is in much better agreement with experiment than that of the static crystal. The first peak of the MD spectrum is much broader than that of the static crystal and more closely matches the experiment. This first peak in the static crystal arises from three p-like states that are separated in energy by $\sim$1 eV (Figs. 3(d) and 3(e)). The relative energies of these states are modified at finite temperature, however, to produce a much broader distribution, and hence a broader spectrum. This is reminiscent of the splitting of the degenerate p-like states in LiF. Additionally, our XCH-MD spectrum has a rather faint s-like (Fig. 3(c)) pre-edge feature at 58.5 eV. This s-like state is also present in the static crystal (Fig. 3(b)), but is centrosymmetric about the excited lithium atom and so does not produce a pre-edge feature, as was the case in LiF. The pre-edge feature is not easily resolved in experiment, although we note that there is a change in slope in the XRS spectrum between 59.2 and 59.5 eV that may indicate the presence of this low lying state.

C. Lithium oxide

So far we have examined the X-ray spectra of ionic lithium compounds, so it is reasonable to ask whether the low lying s-like state found in LiF and Li_2SO_4 is a common feature in the X-ray spectra of all lithium containing compounds, i.e., less ionic lithium compounds. Here, we measure the ionicity of the compound by the character of the bands around the conduction band minimum (CBM): in very ionic compounds, the bands around the CBM would be expected to be dominated by cation (in this case lithium) s character, while in a more covalent compound the cation s-electron is involved in bonding and so features in the valence band maximum. As a test case, we consider lithium oxide (Li_2O), a white (7.99 eV bandgap[63]) solid with the anti-fluorite crystal structure. While bands in the neighborhood of the CBM in LiF comprise $\sim$68% Li $2s$, 24% F $3s$, and 7% Li $2p$ character, respectively (Fig. 4(a)), the more covalent Li_2O has twice as much Li $2p$ and virtually no Li $2s$ character (Fig. 4(b)).

The measured XRS spectrum of Li_2O is characterized by a first main peak at 59.85 eV and a second at 64.56 eV with minor features at 62.4 and 65.63 eV. Overall, we find excellent agreement between the experimental and static crystal spectra (Fig. 5(a)) with all the features of the experiment well reproduced. We find a low-lying s-like state at 58.7 eV in the static crystal, and three p-like states at 60.2 eV that give rise to the first major transition. While this may be reminiscent of LiF, note that the nature of the s-like excited state in Li_2O differs significantly from that of LiF: in Li_2O, the electron density of the first Li $1s$ core-excited state forms a tetragon centered on
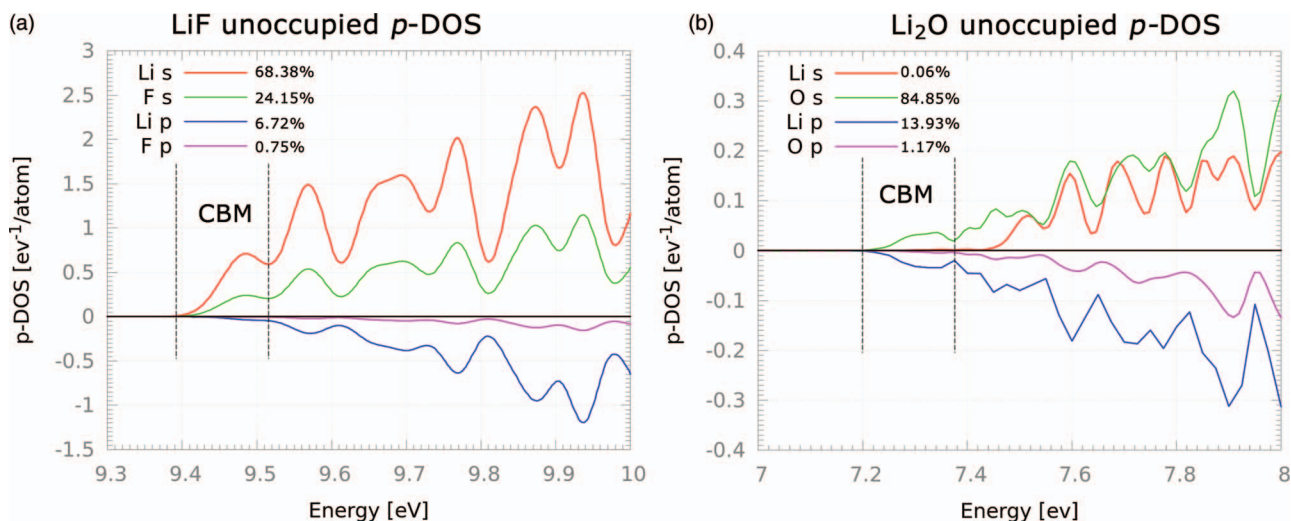
FIG. 4. (a) Unoccupied projected density of states (pDoS) of LiF. We calculated the pDoS using a LiF unit cell and the same pseudopotentials as our XAS calculations and a $20 \times 20 \times 20$ k-point grid. The location of the conduction band minimum (CBM) is indicated and the relative population of the Lithium s (red) and p (blue) and the Fluorine s (green) and p (purple) character calculated by numerical integration to the next available band. (b) The unoccupied pDoS of Li_2O from the crystal unit cell.

the excited Li with each leg oriented towards interstitial sites between triples of coordinating O atoms (Fig. 5(b)).

Our XCH-MD spectrum leads to a spectrum that is broader and in better agreement with experiment. More importantly, and as was seen in the previous lithium compounds, at finite temperature the s-like state is significantly distorted (Figs. 5(b) and 5(e)) with respect to its overlap with the Li $1s$ electron at the atomic nucleus. However, a pre-edge is not observable because the average energy of this s-like state is elevated to 60.2 eV at finite temperature, in the same energy range of the p-like states (59.7–60.5 eV) (Fig. 6(a)). As a result, while this nominally dark s-like state becomes bright

at finite temperature, it ultimately contributes mainly to the first main feature and not a pre-edge feature as in LiF and Li_2SO_4. Of course, the excited Li $1s$ electron couples more strongly to the empty p-like states than to the distorted s-like state which only assumes some p-like character due to instantaneous distortions at finite temperature. With that in mind, re-examination of the aforementioned single distribution of states that give rise to the first major peak in Li_2O reveals two distinct distributions when also sorted by oscillator strength (Fig. 6(b)): excited states from 59.4 to 59.8 eV low oscillator strengths (presumably s-like) and excited states from 59.5 to 60.3 eV with two to three times more oscillator strength
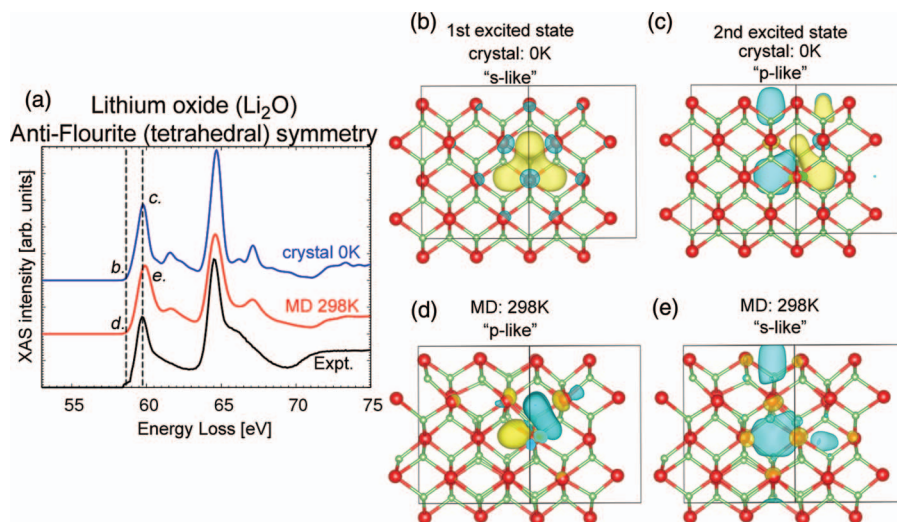

FIG. 5. (a) Comparison of the measured XRS spectrum of Li_2O (black line) with the XCH calculated spectrum using the static crystal (blue) and the ensemble averaged spectrum from 298 K AIMD snapshots (red line). The calculated spectra are both in excellent agreement to experiment. (b) and (c) The first and second electronic excited states of Li_2O calculated from the static crystal. The color scheme for the states is the same as in previous figures. Note that the first excited state is an s-like state with the electron density lying in the interstitial site of the oxygen tetragon formed around each excited Li atom, while the second excited state is a p-like state. (d) and (e) Representative first and second electronic states of Li_2O calculated from snapshots during a 298 K AIMD simulation. The first electronic state is now a p-like state, while the second excited state is an s-like state around the excited Li atom. Note that the s-like state is distorted similar to the ionic compounds studied before, but does not give rise to a pre-edge feature in the Li_2O XAS but rather merges with the lower lying p-like states to give the first major peak at 60 eV.
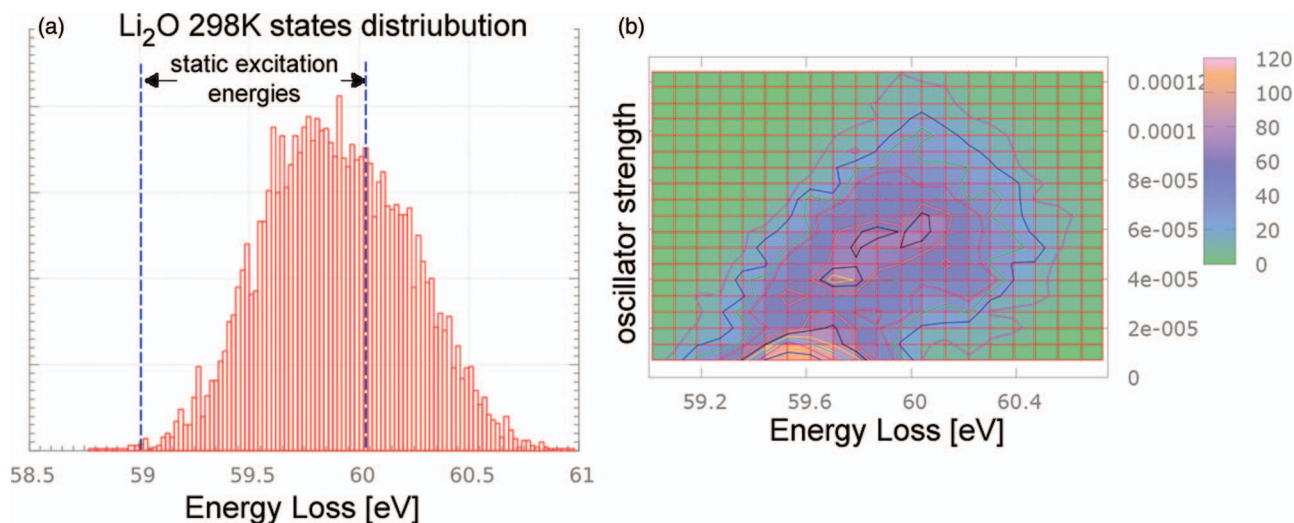
FIG. 6. (a) Distribution of Li_2O excited state energies for each excited Li atom in each of the 10 random AIMD snapshots (960 data points). The excitation energies of the first *s*-like excited state (58.7 eV) and the second *p*-like excited states (60.2 eV) are indicated by the vertical dashed blue lines. At finite temperature, these static energies split into a single broad distribution that manifests as the first major peak around 60 eV. (b) Two-dimensional distribution of the Li_2O excited state energies, ordered by oscillator strength. We find two overlapping distribution of states: states with low oscillator strength at 59.4–59.8 eV are presumably the distorted *s*-like states and states with *p*-like states with higher oscillator strength from 59.5 to 60.3 eV.

(presumably *p*-like). This suggests that while most of the distorted *s*-like states contribute to the first major transition, there could be a weak pre-edge feature from some of the lower lying *s*-like excited states at finite temperature, which could possibly explain the feature in the experimental XRS spectrum from 58.7 to 59.2 eV.

D. Lithium nitride

We now turn our attention to lithium nitride (Li_3N), a 1.3 eV bandgap,[64] layered solid which has hexagonal symmetry. This compound is unique in the set considered in this study in that the lithium in the unit cell are not indistinguishable, but rather occupy two symmetry-distinct sites: intraplanar (forming hexagons around each N atom) and interplanar (connecting N atoms in neighboring planes) (Fig. 7). The experimental spectrum is characterized by an energy onset of 54.93 eV, a first peak at 55 eV, and a second main peak at 61.8 eV, with several broad features from 56–58 and 66–69 eV.

Our calculated spectrum from the static crystal is in excellent agreement with experiment: the first and second main peaks are located at 55.1 and 62.1 eV, respectively. Our XCH spectra is also in excellent agreement with the much more computationally expensive BSE calculations.[65]

One of the advantages of theory is that it can separate the contributions of different atoms in the system, providing information that may be impossible to obtain experimentally. This is particularly suitable for Li_3N, where the two types of lithium have chemical bonding environments, with six and two nitrogen neighbors for the intraplanar and interplanar lithium atoms, respectively. Since XAS is very sensitive to the local chemical bonding geometry, it is reasonable to expect that each type of lithium atom would make different contributions to the XAS spectrum. Our calculations indeed confirm these differences. The first strong peak in the spectrum results from a transition to *p*-like states and is three times as intense for the interplanar as the intraplanar lithium atoms (Fig. 7(b)). We find that the *p*-like states of the interplanar lithium atoms
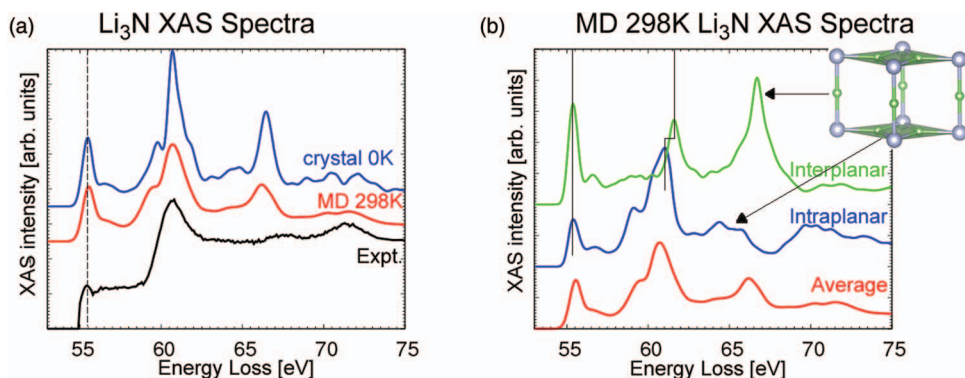

FIG. 7. (a) Comparison of the measured XRS spectrum of Li_3N (black) with the XCH calculated spectrum of the static crystal (blue) and the ensemble averaged spectrum from snapshots during a 298 K AIMD simulation. (b) Comparison of the interplanar (green) and intraplanar (blue) spectrum of Li_3N (red). Inset: The Li_3N unit cell displaying hexagonal symmetry. The interplanar and intraplanar Li atoms are indicated.
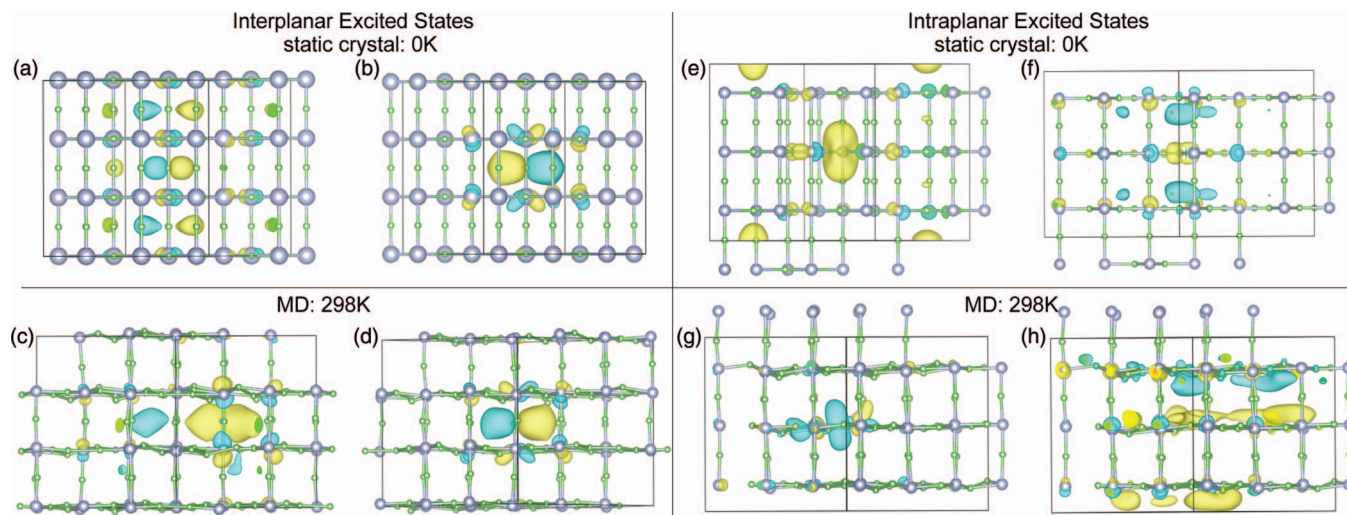
FIG. 8. Representative electronic excited states responsible for the first two major features in Li_3N for the interplanar (a)–(d) and intraplanar (e)–(h) lithium atoms in Li_3N from the static crystal (a), (b), (e), and (f) and from snapshots of our 298 K AIMD simulation (c), (d), (g), and (h).

are fairly localized about the excited lithium (Figs. 8(a)–8(d)), while those of the intraplanar lithium atoms delocalized over the hexagonal rings (Figs. 8(e)–8(h)). Interestingly, the first excited state of the intraplanar lithium atom is an *s*-like state in the static crystal (Fig. 8(e)) that acquires *p* character due to instantaneous distortions of the crystal lattice (8g), enhancing the intensity of the first feature in the MD sampled spectrum.

E. Lithium carbonate

So far we have demonstrated that ΔSCF calculations in the XCH formalism predict XAS in excellent agreement with high-resolution experiments. One may ask what the practical limits of this approach are, and whether MD sampling necessarily leads to better spectra in more complex materials. We begin to answer this by considering lithium carbonate, a monoclinic crystal (inset of Fig. 9). As shown in Fig. 9,
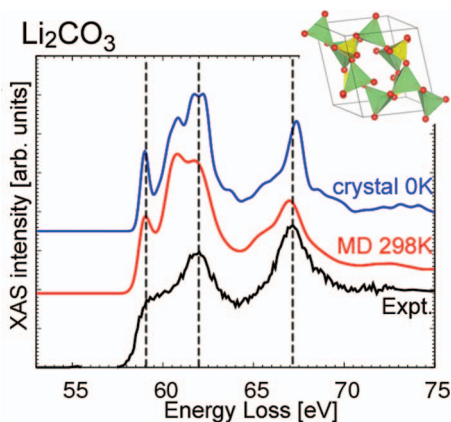
FIG. 9. Comparison of the measured XRS spectrum of Li_2CO_3 (black) with the XCH calculated spectrum of the static crystal (blue) and the ensemble averaged spectrum from snapshots during a 298 K AIMD simulation. The major features are indicated by vertical dashed lines to guide the eyes. Overall, we find excellent agreement with the peak position, although some features are much more prominent in the calculated spectrum than in experiment. Inset. The Li_2CO_3 monoclinic unit cell.

the experimental spectrum is characterized by major features at 61.8 and 67.9 eV. Our XCH spectra are in reasonable agreement with the experiment, with predicted first and second major peaks at 62.7 eV and 68.3 eV, respectively. Both the static crystal and the MD sampled spectra predict a significant feature at 59.1 eV, however, that cannot be resolved in the experiment. Neglecting possible errors in the experimental measurements due to beam damage or sample contamination (possibly due to the presence of water[66]), the disagreement between experiment and theory could arise from quadrupole contributions, although they should be quite small in the experimental measurements. A previous study of Li_2CO_3 using the Bethe-Salpeter approach[13] showed that the intensity of this pre-edge feature changes dramatically within momentum transfer magnitude q. We are currently working on extending our approach to include quadrupole contributions. We would expect that our calculations are well converged with respect to supercell size. While calculations with larger supercells could potentially modify the absorption edge, we note that the $2 \times 3 \times 3$ supercell used in our calculation already contains 432 atoms, and is the largest supercell considered in this study. Thus, calculations with larger supercells, while feasible, are not practicable within the MD sampling scheme.

IV. CONCLUSIONS

The XRS spectra of lithium compounds are diverse, due to their wide range of Li bonding, coordination, and crystal symmetries. In this study, we applied ΔSCF calculations in the XCH to calculate the X-ray absorption spectra of lithium fluoride, sulfate, oxide, nitride, and carbonate and compared these simulated spectra to high resolution X-ray Raman measurements. Our approach produces spectra in very good to excellent agreement with high-resolution XRS measurements. An often ignored, but important, consideration in these calculations is the role of temperature in modifying the energy levels and character of the excited states. We have demonstrated over a class of compounds that atomic distortions can

lead to non-centrosymmetric excited states that overlap significantly with the lithium $1s$ core electron wave function, and, in the more ionic lithium compounds, produce pre-edge, weakly allowed transitions which would be dipole forbidden in the static crystal. In addition to validating the predictive power of theoretical X-ray calculations, these results provide an accurate and efficient benchmark study for identification and characterization of Li compounds and their temperature dependent dynamical properties. This newly developed ability will be of crucial importance when interpreting spectra resulting from complex reactions, which typically lead to mixtures of compounds, and form newly formed compounds in extreme conditions, such as under electrochemical potentials or high pressures. One can more readily envisage using X-ray absorption/Raman spectroscopy for the study of technologically relevant processes, in batteries or hydrogen storage devices, under working conditions. This study also opens the door to the possibility of studying dynamic, time dependent phenomena, such as ion conduction, in materials using X-ray absorption/Raman spectroscopy.

ACKNOWLEDGMENTS

[1]S. I. Orimo, Y. Nakamori, J. R. Eliseo, A. Zuttel, and C. M. Jensen, Chem. Rev. **107**(10), 4111 (2007).

[2]P. Chen, Z. T. Xiong, J. Z. Luo, J. Y. Lin, and K. L. Tan, Nature (London) **420**(6913), 302 (2002).

[3]H. Li, Z. X. Wang, L. Q. Chen, and X. J. Huang, Adv. Mater. **21**(45), 4593 (2009).

[4]F. Wang, H. C. Yu, M. H. Chen, L. J. Wu, N. Pereira, K. Thornton, A. Van der Ven, Y. M. Zhu, G. G. Amatucci, and J. Graetz, Nat. Commun. **3**, 8 (2012).

[5]G. Barkhordarian, T. Klassen, M. Dornheim, and R. Bormann, J. Alloys Compd. **440**(1), L18 (2007); L. L. Shaw, X. Wan, J. Z. Hu, J. H. Kwak, and Z. Yang, J. Phys. Chem. C **114**(17), 8089 (2010).

[6]R. Marom, S. F. Amalraj, N. Leifer, D. Jacob, and D. Aurbach, J. Mater. Chem. **21**(27), 9938 (2011).

[7]S. Q. Shi, P. Lu, Z. Y. Liu, Y. Qi, L. G. Hector, H. Li, and S. J. Harris, J. Am. Chem. Soc. **134**(37), 15476 (2012).

[8]J. Stöhr, *NEXAFS Spectroscopy* (Springer-Verlag, Berlin, 1992).

[9]F. de Groot, Chem. Rev. **101**(6), 1779 (2001).

[10]F. Gel'mukhanov and H. Ågren, Phys. Rep. **312**(3), 87 (1999); T. Suzuki, J. Phys. Soc. Jpn. **22**(5), 1139 (1967).

[11]K. Tohji and Y. Udagawa, Phys. Rev. B **39**(11), 7590 (1989); **36**(17), 9410 (1987); M. H. Krisch, F. Sette, C. Masciovecchio, and R. Verbeni, Phys. Rev. Lett. **78**(14), 2843 (1997); U. Bergmann, O. C. Mullins, and S. P. Cramer, Anal. Chem. **72**(11), 2609 (2000).

[12]D. Sokaras, D. Nordlund, T. C. Weng, R. A. Mori, P. Velikov, D. Wenger, A. Garachtchenko, M. George, V. Borzenets, B. Johnson, Q. Qian, T. Rabedeau, and U. Bergmann, Rev. Sci. Instrum. **83**(4), 043112 (2012).

[13]T. T. Fister, M. Schmidt, P. Fenter, C. S. Johnson, M. D. Slater, M. K. Y. Chan, and E. L. Shirley, J. Chem. Phys. **135**(22), 224513 (2011).

[14]A. Andersson, D. Abraham, R. Haasch, S. MacLaren, J. Liu, and K. Amine, J. Electrochem. Soc. **149**(10), A1358 (2002); M. Balasubramanian, H. S. Lee, X. Sun, X. Yang, A. Moodenbaugh, J. McBreen, D. Fischer, and Z. Fu, Electrochem. Solid-State Lett. **5**(1), A22 (2002).

[15]D. Aurbach, J. Power Sources **89**(2), 206 (2000).

[16]J. B. Goodenough and Y. Kim, Chem. Mater. **22**(3), 587 (2010); E. Peled, J. Electrochem. Soc. **126**(12), 2047 (1979).

[17]B. D. McCloskey, D. S. Bethune, R. M. Shelby, G. Girishkumar, and A. C. Luntz, J. Phys. Chem. Lett. **2**(10), 1161 (2011).

[18]D. Prendergast and G. Galli, Phys. Rev. Lett. **96**(21), 215502 (2006).

[19]J. S. Uejio, C. P. Schwartz, R. J. Saykally, and D. Prendergast, Chem. Phys. Lett. **467**(1–3), 195 (2008).

[20]A. H. England, A. M. Duffin, C. P. Schwartz, J. S. Uejio, D. Prendergast, and R. J. Saykally, Chem. Phys. Lett. **514**(4–6), 187 (2011).

[21]J. Cabana, L. Monconduit, D. Larcher, and M. R. Palacin, Adv. Mater. **22**(35), E170 (2010).

[22]M. Armand and J. M. Tarascon, Nature (London) **451**(7179), 652 (2008); A. Züttel, P. Wenger, S. Rentsch, P. Sudan, P. Mauron, and C. Emmenegger, J. Power Sources **118**(1), 1 (2003).

[23]D. Maganas, M. Roemelt, M. Havecker, A. Trunschke, A. Knop-Gericke, R. Schlogl, and F. Neese, Phys. Chem. Chem. Phys. **15**(19), 7260 (2013).

[24]E. L. Shirley, Phys. Rev. Lett. **80**(4), 794 (1998); J. Electron Spectrosc. Relat. Phenom. **144–147**, 1187 (2005); W. Olovsson, I. Tanaka, P. Puschnig, and C. Ambrosch-Draxl, J. Phys.: Condens. Matter **21**(10), 104205 (2009); J. Vinson, J. Kas, F. Vila, J. Rehr, and E. Shirley, Phys. Rev. B **85**(4), 045101 (2012).

[25]M. Haverkort, M. Zwierzycki, and O. Andersen, Phys. Rev. B **85**(16), 165113 (2012).

[26]W. H. E. Schwarz and R. J. Buenker, Chem. Phys. **13**(2), 153 (1976).

[27]N. A. Besley, A. T. B. Gilbert, and P. M. W. Gill, J. Chem. Phys. **130**(12), 124308 (2009).

[28]J. C. Slater and K. H. Johnson, Phys. Rev. B **5**(3), 844 (1972); J. C. Slater, Adv. Quantum Chem. **6**(1), 92 (1972).

[29]B. Hetenyi, F. De Angelis, P. Giannozzi, and R. Car, J. Chem. Phys. **120**(18), 8632 (2004).

[30]S.-D. Mo and W. Y. Ching, Phys. Rev. B **62**(12), 7901 (2000).

[31]K. A. Jackson and M. R. Pederson, Phys. Rev. Lett. **67**(18), 2521 (1991).

[32]C. P. Schwartz, J. S. Uejio, A. M. Duffin, A. H. England, D. Prendergast, and R. J. Saykally, J. Chem. Phys. **131**(11), 114509 (2009).

[33]D. Prendergast and S. G. Louie, Phys. Rev. B **80**(23), 235126 (2009).

[34]E. L. Shirley, Phys. Rev. B **54**(23), 16464 (1996).

[35]L. Kong, X. Wu, and R. Car, Phys. Rev. B **86**(13), 134203 (2012).

[36]A. J. Cohen, P. Mori-Sanchez, and W. T. Yang, Phys. Rev. B **77**(11), 115123 (2008); P. Mori-Sanchez, A. J. Cohen, and W. T. Yang, Phys. Rev. Lett. **100**(14), 146401 (2008).

[37]F. Fuchs, J. Furthmüller, F. Bechstedt, M. Shishkin, and G. Kresse, Phys. Rev. B **76**(11), 115109 (2007); W. G. Aulbur, L. Jonsson, and J. W. Wilkins, Solid State Phys.: Adv. Res. Appl. **54**, 1 (2000).

[38]C. P. Schwartz, J. S. Uejio, A. M. Duffin, A. H. England, D. N. Kelly, D. Prendergast, and R. J. Saykally, Proc. Natl. Acad. Sci. U.S.A. **107**(32), 14008 (2010).

[39]J. S. Uejio, C. P. Schwartz, A. M. Duffin, A. England, D. Prendergast, and R. J. Saykally, J. Phys. Chem. B **114**(13), 4702 (2010).

[40]J. P. Perdew, K. Burke, and M. Ernzerhof, Phys. Rev. Lett. **77**(18), 3865 (1996).

[41]D. Vanderbilt, Phys. Rev. B **41**(11), 7892 (1990).

[42]P. Giannozzi, S. Baroni, N. Bonini, M. Calandra, R. Car, C. Cavazzoni, D. Ceresoli, G. L. Chiarotti, M. Cococcioni, and I. Dabo, J. Phys.: Condens. Matter **21**(39), 395502 (2009).

[43]M. Taillefumier, D. Cabaret, A.-M. Flank, and F. Mauri, Phys. Rev. B **66**(19), 195107 (2002).

[44]P. Jiang, D. Prendergast, F. Borondics, S. Porsgaard, L. Giovanetti, E. Pach, J. Newberg, H. Bluhm, F. Besenbacher, and M. Salmeron, J. Chem. Phys. **138**(2), 024704 (2013).

[45]M. Teruyasu, T. Isao, G. Shang-Peng, and J. P. Chris, J. Phys.: Condens. Matter **21**(10), 104204 (2009).

[46]G. Lippert, J. Hutter, and M. Parrinello, Mol. Phys. **92**(3), 477 (1997).

[47]J. VandeVondele, M. Krack, F. Mohamed, M. Parrinello, T. Chassaing, and J. Hutter, Comput. Phys. Commun. **167**(2), 103 (2005).

[48]J. VandeVondele and J. Hutter, J. Chem. Phys. **127**(11), 114105 (2007).

[49]S. Goedecker, M. Teter, and J. Hutter, Phys. Rev. B **54**(3), 1703 (1996); M. Krack, Theor. Chem. Acc. **114**(1–3), 145 (2005).

[50]L. Genovese, T. Deutsch, and S. Goedecker, J. Chem. Phys. **127**(5), 054704 (2007).

[51]A. B. Kunz, Phys. Rev. B **26**(4), 2056 (1982); F. J. Himpsel, L. J. Terminello, D. A. Lapianosmith, E. A. Eklund, and J. J. Barton, Phys. Rev. Lett. **68**(24), 3611 (1992).

[52]P. Verma, P. Maire, and P. Novak, Electrochim. Acta **55**(22), 6332 (2010).

[53]J. Tsuji, H. Nakamatsu, T. Mukoyama, K. Kojima, S. Ikeda, and K. Taniguchi, X-Ray Spectrum. **31**(4), 319 (2002).

[54]B. F. Sonntag, Phys. Rev. B **9**(8), 3601 (1974).

[55]A. B. Kunz, J. T. Devreese, and T. Collins, J. Phys. C: Solid State Phys. **5**(22), 3259 (1972); S. T. Pantelides and F. C. Brown, Phys. Rev. Lett. **33**(5), 298 (1974); A. B. Kunz, Phys. Rev. B **12**(12), 5890 (1975); S. T. Pantelides, Phys. Rev. B **11**(6), 2391 (1975).

[56]J. R. Fields, P. C. Gibbons, and S. E. Schnatterly, Phys. Rev. Lett. **38**(8), 430 (1977).

[57]G. I. Finch and S. Fordham, Proc. Phys. Soc. **48**, 85 (1936).

[58]E. S. Božin, C. D. Malliakas, P. Souvatzis, T. Proffen, N. A. Spaldin, M. G. Kanatzidis, and S. J. L. Billinge, Science **330**(6011), 1660 (2010).

[59]C. Catlow, K. Diller, and L. Hobbs, Philos. Mag. A **42**(2), 123 (1980).

[60]K. Schwartz, in *Atomic Physics Methods in Modern Research*, edited by K. Jungmann, J. Kowalski, I. Reinhard, and F. Träger (Springer, Berlin, Heidelberg, 1997), Vol. 499, pp. 351.

[61]J. G. Albright, Z. Kristallogr. **84**(1/2), 150 (1932).

[62]R. W. Impey, M. L. Klein, and I. R. McDonald, J. Chem. Phys. **82**(10), 4690 (1985).

[63]J. M. Bijvoet, A. Claassen, and A. Karssen, Proc. Konin. Akad. Wetensch. Amsterdam **29**(1/5), 529 (1926).

[64]A. Lazicki, B. Maddox, W. Evans, C. S. Yoo, A. McMahan, W. Pickett, R. Scalettar, M. Hu, and P. Chow, Phys. Rev. Lett. **95**(16), 165503 (2005).

[65]T. T. Fister, G. T. Seidler, E. L. Shirley, F. D. Vila, J. J. Rehr, K. P. Nagle, J. C. Linehan, and J. O. Cross, J. Chem. Phys. **129**(4), 044702 (2008).

[66]K. Edström, M. Herstedt, and D. P. Abraham, J. Power Sources **153**(2), 380 (2006).

[67]A. Rabenau and H. Schulz, J. Less-Common Metals **50**(1), 155 (1976).

[68]J. Zemann, Acta Crystallogr. **10**(10), 664 (1957).

[69]Y. Ishii, J. Murakami, and M. Itoh, J. Phys. Soc. Jpn. **68**(2), 696 (1999).